

Dark-ages reionization & galaxy formation simulation IV: UV luminosity functions of high-redshift galaxies

Chuanwu Liu^{1*}, Simon J. Mutch¹, P. W. Angel¹, Alan R. Duffy^{2,1}, Paul M. Geil¹
 Gregory B. Poole¹, Andrei Mesinger³ and J. Stuart B. Wyithe¹

¹*School of Physics, University of Melbourne, Parkville, VIC 3010, Australia*

²*Centre for Astrophysics & Supercomputing, Swinburne University of Technology, PO Box 218, Hawthorn, VIC 3122, Australia*

³*Scuola Normale Superiore, Piazza dei Cavalieri 7, I-56126 Pisa, Italy*

28 April 2016

ABSTRACT

In this paper we present calculations of the UV luminosity function from the Dark-ages Reionization And Galaxy-formation Observables from Numerical Simulations (DRAGONS) project, which combines N-body, semi-analytic and semi-numerical modelling designed to study galaxy formation during the Epoch of Reionization. Using galaxy formation physics including supernova feedback, the model naturally reproduces the UV LFs for high-redshift star-forming galaxies from $z\sim 5$ through to $z\sim 10$. We investigate the luminosity–star formation rate (SFR) relation, finding that variable SFR histories of galaxies result in a scatter around the median relation of 0.1–0.3 dex depending on UV luminosity. We find close agreement between the model and observationally derived SFR functions. We use our calculated luminosities to investigate the luminosity function below current detection limits, and the ionizing photon budget for reionization. We predict that the slope of the UV LF remains steep below current detection limits and becomes flat at $M_{UV}\gtrsim -14$. We find that 48 (17) per cent of the total UV flux at $z\sim 6$ (10) has been detected above an observational limit of $M_{UV}\sim -17$, and that galaxies fainter than $M_{UV}\sim -17$ are the main source of ionizing photons for reionization. We investigate the luminosity–stellar mass relation, and find a correlation for galaxies with $M_{UV}<-14$ that has the form $M_*\propto 10^{-0.47M_{UV}}$, in good agreement with observations, but which flattens for fainter galaxies. We determine the luminosity–halo mass relation to be $M_{vir}\propto 10^{-0.35M_{UV}}$, finding that galaxies with $M_{UV}=-20$ reside in host dark matter haloes of $10^{11.0\pm 0.1}M_\odot$ at $z\sim 6$, and that this mass decreases towards high redshift.

Key words: galaxies: high redshift – galaxies: evolution – galaxies: formation – galaxies: luminosity function, mass function

1 INTRODUCTION

The luminosity function (LF) is one of the most fundamental observables for high-redshift galaxies. The intrinsic UV continuum of galaxies is determined by young stellar populations, and is therefore thought to be a good tracer for understanding the star-formation processes in galaxies. As a result, measurement of the UV LF constrains the buildup of stellar mass in the high-redshift Universe and the role of galaxies in reionization. Successfully describing the UV LF of high-redshift galaxies is therefore essential for any model aiming to understand galaxy formation at high redshift.

The hierarchical structure formation scenario (White &

Rees 1978) in a dark energy and cold dark matter (Λ CDM) universe can simultaneously explain a wide variety of observational features, and is the currently favoured cosmological model. In this model, galaxies form in the potential wells of dark matter haloes, where accreted, shock heated gas cools and condenses into star-forming disks (Fall & Efstathiou 1980). Semi-analytic models have had considerable success in reproducing galaxy-formation observables based on this scenario (White & Frenk 1991; Kauffmann et al. 1993; Cole et al. 1994; Kauffmann et al. 1999; Cole et al. 2000; Croton et al. 2006; Bower et al. 2006; Somerville et al. 2008; Lacey et al. 2011; Mutch et al. 2013; Lacey et al. 2015).

A typical semi-analytic model consists of numerical and analytic parts: (i) N-body simulations are used to generate the formation and merger history of dark matter haloes; (ii)

* E-mail: chuanwul@student.unimelb.edu.au

The interplay amongst the baryonic, stellar and gas components are modelled analytically within these dark matter structures; (iii) The observable features, such as the luminosities and colours are evaluated by stellar population synthesis (e.g. Bruzual & Charlot 2003; Gonzalez-Perez et al. 2014). When compared with hydrodynamical simulations (e.g. Schaye et al. 2010, 2015) semi-analytic models are far less computationally expensive, since they process the dark-matter-dominated large-scale structure formation and computationally intensive baryon-dominated galaxy formation separately. On the other hand, semi-analytic models sacrifice a detailed description of the gas physics, and rely on empirical or idealized laws for galaxy formation properties.

Feedback is extremely important for the formation and evolution of galaxies. Supernovae and active galactic nuclei (AGN) are typically the two dominant modes of feedback incorporated in semi-analytic models (e.g. Baugh 2006). Apart from this internal feedback within galaxies, the UV background (UVB) radiation also heats the intergalactic medium (IGM) and can reduce the infall of gas into the shallow potential wells of small haloes. This UV photo-ionization feedback mechanism delays the completion of reionization and suppresses the baryon content and star-formation rate (SFR) of small galaxies (Sobacchi & Mesinger 2013b,a). Therefore, including the UVB feedback for individual galaxies is necessary for accurately modelling galaxy formation during the Epoch of Reionization (EoR).

This is the fourth paper in a series describing the Dark-ages Reionization And Galaxy-formation Observables from Numerical Simulation (DRAGONS¹) project, which is based on high resolution and high cadence N-body simulations *Tiamat* (Poole et al. 2015, hereafter Paper-I; Angel et al. 2015, Paper-II), and the semi-analytic MERAXES model of galaxy formation (Mutch et al. 2015, hereafter Paper-III), which has been integrated with a semi-numerical algorithm for ionization structure (Mesinger & Furlanetto 2007). The aim of this paper is to use stellar population synthesis to characterize the UV LF of high-redshift galaxies from MERAXES, and to study the ionizing photon budget for reionization. The luminosity dependence of a variety of intrinsic galaxy properties is also studied.

Galaxies at high redshift are too faint to be observed spectroscopically. However, they can be identified using multi-band photometry and selected using the Lyman-break technique (Steidel et al. 1996). Using this technique, significant progress has been made in the past two decades in characterizing the observed UV LF of galaxies towards higher redshifts (Steidel et al. 1999; Bouwens et al. 2007, 2010; Oesch et al. 2010; McLure et al. 2010; Bouwens et al. 2011; Finkelstein et al. 2012; Schenker et al. 2013; McLure et al. 2013; Duncan et al. 2014; Schmidt et al. 2014; Bouwens et al. 2014a). The most comprehensive UV LF measurements to date at $z > 4$ were made by Bouwens et al. (2015b) and Bouwens et al. (2015c), based on the assembly of HST datasets including CANDELS, HUDF09, HUDF12, ERS and BORG/HIPPIES programs. The large number (> 10000) of galaxies at $z \geq 4$ provide statistically reliable UV LFs for testing our semi-analytic model of galaxy formation during the reionization era.

Young galaxies are strong emitters of UV radiation. High-redshift galaxies are therefore thought to be a significant sources of reionizing photons. However, galaxies above current detection limits (e.g., an absolute UV magnitude $M_{UV} \sim -17$ at $z \sim 6$) are not sufficiently numerous to maintain reionization. Rather, empirical studies and simulations show a galaxy population down to $M_{UV} = -13$ is required (e.g. Robertson et al. 2013; Duffy et al. 2014; Robertson et al. 2015; Bouwens et al. 2015a). The faint-end slope of UV LFs is therefore very important since it determines the number of reionizing photons emitted from the faint galaxies below current detection limits. On the other hand, theoretically, we expect that baryons in very low-mass dark matter haloes ($\lesssim 10^8 M_{\odot}$) cannot efficiently cool and form stars, implying that the LFs may have a truncation at a very faint luminosity.

Observational and numerical studies have investigated the shape of the UV LF at faint luminosities. Atek et al. (2015) recently obtained LFs down to $M_{UV} = -15.25$ at $z \sim 7$ behind lensing clusters, and found that the faint-end slope remains steep. Using the star-formation histories of Local Group dwarf galaxies obtained from a color-magnitude diagram analysis, Weisz et al. (2014) inferred the LF at $z \sim 5$ down to $M_{UV} \sim -5$, and found no truncation. In contrast, using high-resolution cosmological hydrodynamic simulations, Wise et al. (2014) found the slope of LFs at $z > 7$ is flat at $M_{UV} > -12$. Further, O’Shea et al. (2015) found that the slope is flat for faint luminosities at $z > 12$ from calculations with a larger simulation volume. The DRAGONS simulation provides a framework within which we can consider the faint end of the LF within a self-consistent calculation of the reionization history.

This paper is organized as follows. We first summarize our stellar population synthesis modelling as well as the Lyman-break colour selection criteria in Section 2. We then show our results for the observed UV LF of selected galaxies in Section 3. In Section 4, we calculate the fraction of total UV flux above observed luminosity limits. We study the relation between UV luminosity and properties of galaxies including SFR and galaxy stellar mass, as well as the mass of dark matter haloes in Section 5. Finally, in Section 6, we present our conclusions. We employ a standard spatially-flat Λ CDM cosmology based on *Planck* 2015 data (Planck Collaboration et al. 2015): $(h, \Omega_m, \Omega_b, \Omega_{\Lambda}, \sigma_8, n_s) = (0.678, 0.308, 0.0484, 0.692, 0.815, 0.968)$. All magnitudes are presented in the AB system (Oke & Gunn 1983).

2 MODELLING UV LUMINOSITIES

The galaxy formation model used in this work is MERAXES (Paper-III), a new semi-analytic model with updated physics based on Croton et al. (2006). MERAXES is implemented on dark matter halo merger trees generated from the N-body simulation *Tiamat* described in Paper-I. Our fiducial model is based on the *Tiamat* simulation, which is run in a $67.8 h^{-1} \text{Mpc}$ (comoving) cube box including 2160^3 particles with a particle mass of $2.64 \times 10^6 h^{-1} M_{\odot}$.

Tiamat and MERAXES have been designed for studies of reionization. We have performed halo finding on 100 snapshots at $z \geq 5$, and thus constructed merger trees with a cadence of one snapshot per $\sim 10^7$ years. This resolves the

¹ <http://dragons.ph.unimelb.edu.au>

dynamical time of galaxy disks at high redshift, and represents a time resolution comparable to the lifetime of massive stars, allowing us to include time-resolved supernova feedback. The merger trees are “horizontally” constructed so that the semi-analytic model computes properties of all galaxies at each consecutive snapshot. This allows us to implement a self-consistent calculation of feedback from reionization.

Some basic characteristics of the MERAXES semi-analytic model are described below (for a detailed description of MERAXES see Paper-III):

(i) Cooling: Gas infalling into a halo is assumed to be shocked to the virial temperature of the halo $T=3.59 \times 10^5 (V_{\text{vir}}/100 \text{ km s}^{-1})^2 \text{ K}$, where V_{vir} is the virial velocity. The hot gas can subsequently cool via a number of mechanisms, with a cooling time at radius r of

$$t_{\text{cool}}(r) = \frac{3}{2} \frac{\bar{\mu} m_p k T}{\rho_{\text{hot}}(r) \Lambda(T, Z)}, \quad (1)$$

where $\bar{\mu} m_p$ is the mean particle mass, k is the Boltzmann constant, ρ_{hot} is the hot gas density, and $\Lambda(T, Z)$ is the cooling function (Sutherland & Dopita 1993) which depends on both the temperature and metallicity of the gas. The hot gas density is assumed to have a simple isothermal spherical distribution:

$$\rho_{\text{hot}} = \frac{m_{\text{hot}}}{4\pi R_{\text{vir}} r^2}. \quad (2)$$

The cooling radius, r_{cool} , is defined as the radius at which t_{cool} is equal to the dynamical time of the halo, $t_{\text{dyn}}=R_{\text{vir}}/V_{\text{vir}}$ (Croton et al. 2006). The gas enclosed within r_{cool} has sufficient time to cool and flow to the centre. For haloes which have $r_{\text{cool}} \geq R_{\text{vir}}$, hot gas directly cools into the central regions of haloes. For haloes which have $r_{\text{cool}} < R_{\text{vir}}$, a quasi-static hot atmosphere will form. The mass cooling rate is determined by:

$$\begin{aligned} \dot{m}_{\text{cool}} &= 4\pi \rho_{\text{hot}}(r_{\text{cool}}) r_{\text{cool}}^2 \dot{r}_{\text{cool}} \\ &= \frac{1}{2} m_{\text{hot}} \frac{r_{\text{cool}} V_{\text{vir}}}{R_{\text{vir}}^2}. \end{aligned} \quad (3)$$

(ii) Star formation: Cold gas in the central regions of haloes is assumed to settle into a rotationally supported disk with a size $r_{\text{disk}}=(3\lambda/\sqrt{2})R_{\text{vir}}$, where λ is the spin parameter of the halo (Mo et al. 1998; Croton et al. 2006). Star formation is assumed to occur if the total amount of cold gas in the disk exceeds a critical value:

$$m_{\text{crit}} = 2\pi \Sigma_{\text{norm}} \left(\frac{V_{\text{vir}}}{\text{kms}^{-1}} \right) \left(\frac{r_{\text{disk}}}{\text{kpc}} \right) 10^6 M_{\odot}, \quad (4)$$

where Σ_{norm} is a free parameter in MERAXES. The SFR in the disk is then given by

$$\dot{m}_{*} = \alpha_{\text{SF}} \frac{m_{\text{cold}} - m_{\text{crit}}}{t_{\text{dyn}}^{\text{disk}}}, \quad (5)$$

where $t_{\text{dyn}}^{\text{disk}}=r_{\text{disk}}/V_{\text{vir}}$ is the disk dynamical time and α_{SF} is a free parameter describing the star-formation efficiency. Galaxy mergers can drive strong turbulence in cold gas and trigger a burst of star formation. The fraction of total cold gas consumed during the burst is (Somerville et al. 2001)

$$e_{\text{burst}} = \alpha_{\text{burst}} (m_{\text{small}}/m_{\text{big}})^{\gamma_{\text{burst}}}, \quad (6)$$

where $m_{\text{small}}/m_{\text{big}}$ is the mass ratio of the merging galaxies, and $\alpha_{\text{burst}} = 0.56$ and $\gamma_{\text{burst}} = 0.7$. The assumed initial

stellar mass function (IMF) in our semi-analytic model is a standard Salpeter (1955) IMF of the form $\phi \propto m^{-2.35}$ in the mass range $0.1 M_{\odot} \leq m \leq 120 M_{\odot}$.

(iii) Delayed supernova feedback: MERAXES includes internal galaxy feedback from type II supernovae. Stars with mass greater than $8 M_{\odot}$ will end their lives as type II supernovae and release mass and energy. In many semi-analytic models (e.g. those based on the Millennium Simulation; Springel et al. 2005), the separation between each simulation snapshot is large, and an assumption of instantaneous supernova feedback is used, with energy and mass released as soon as the relevant stars are formed. However, *Tiamat* has a much higher time resolution of $\sim 11 \text{ Myr}$ in order to resolve the shorter galaxy dynamical time at high redshift. An $8 M_{\odot}$ star, which lives $\sim 40 \text{ Myr}$ will therefore explode $\sim 3\text{--}4$ snapshots after it formed. For this reason MERAXES implements a delayed supernova feedback scheme, where a supernova may explode several snapshots after the star-formation episode.

(iv) UVB photo-evaporation: MERAXES includes UVB photo-suppression feedback, which leads to a reduced baryon fraction, f_{mod} , in individual host dark matter haloes relative to the global baryon fraction $f_b=\Omega_b/\Omega_m$ (Sobacchi & Mesinger 2013b):

$$f_{\text{mod}}(M_{\text{vir}}) = 2^{-M_{\text{crit}}/M_{\text{vir}}}, \quad (7)$$

where M_{vir} is the mass of the halo, M_{crit} is the critical halo mass at which $f_{\text{mod}} = 0.5$:

$$M_{\text{crit}} = M_0 J_{21}^a \left(\frac{1+z}{10} \right)^b \left[1 - \left(\frac{1+z}{1+z_{\text{ion}}} \right)^c \right]^d, \quad (8)$$

where J_{21} is the local ionizing intensity, z_{ion} is the redshift at which the halo was first exposed to the UVB and $(M_0, a, b, c, d)=(2.8 \times 10^9 M_{\odot}, 0.17, -2.1, 2.0, 2.5)$ are best fit parameters as found by Sobacchi & Mesinger (2013b). MERAXES embeds a modified version of the code 21CMFAST (Mesinger et al. 2011) in order to construct the ionization field, and to calculate z_{ion} and the average UVB intensity, $\langle J_{21} \rangle$.

The free parameters in MERAXES were calibrated to replicate the observed stellar mass function at $z \sim 5\text{--}7$ (González et al. 2011; Duncan et al. 2014; Grazian et al. 2015; Song et al. 2015), as well as the *Planck* optical depth to electron scattering measurements (Planck Collaboration et al. 2015).

2.1 Stellar population synthesis

Galaxies contain populations of stars with different ages, which form in one or more progenitor galaxies. From a galaxy at a specific redshift z_0 , we trace all progenitors in the merger tree and calculate their total SFR at each snapshot redshift z_i ($z_i > z_0$). The stars formed at z_i have an age of

$$\tau = t - t' = t(z_0) - t(z_i),$$

where $t(z)$ is the age of the Universe at redshift z . Through this process, we build a star-formation history as a function of time, $\Psi(t)$, for the observed galaxy. Because of the short dynamical time at high redshift, the starburst can result in a rapid change in UV flux during a single snapshot.

Rather than begin the burst at the beginning or end of the snapshot, we therefore interpolate over 10 timesteps between each snapshot assuming a constant SFR rate. We find that our results are insensitive to the precise number of sub-steps.

For a ‘normal’ galaxy without a significant active galactic nucleus, the intrinsic (unattenuated) stellar luminosity at the rest-frame wavelength λ is

$$L_\lambda = \int_0^t \Psi(t') \mathcal{L}_\lambda(t-t') dt', \quad (9)$$

where $\mathcal{L}_\lambda(\tau)$ is the luminosity per unit stellar mass of the coeval population with stellar age τ , and Ψ is the star-formation history.

In this paper, model stellar energy distributions (SEDs) are generated using the public software package STAR-BURST99 (Leitherer et al. 1999; Vázquez & Leitherer 2005; Leitherer et al. 2010, 2014) with a Salpeter IMF in the mass range 0.1–120 M_\odot in order to be consistent with the calculation of SFR in MERAXES. The Geneva evolutionary tracks with standard mass loss are selected. The metallicity is set to $Z=0.001$ (0.05 Z_\odot), which is appropriate during the EoR. Although MERAXES computes the evolution in metallicity of the interstellar medium, for clarity we have taken the simple approach of a single constant metallicity value for star formation. We have checked that assuming metallicity values in the range $0.001 < Z < 0.008$ does not significantly affect our results. We do not include nebular components as they would not affect the UV luminosities of our model galaxies.

2.2 Lyman- α absorption

The spectrum of UV radiation from a high-redshift galaxy passing through intergalactic gas clouds which contain neutral hydrogen will show a series of Ly α absorption lines at wavelengths shorter than $\lambda=1216(1+z)\text{\AA}$. The fraction of neutral hydrogen in the IGM grows rapidly towards high redshifts and the Ly α absorption optical depth is observed to significantly increase, with the SED of high- z star-forming galaxies showing a dropout at $1216(1+z)\text{\AA}$. These galaxies are therefore called Lyman-break galaxies (LBGs, Steidel et al. 1996).

To mimic the LBG selection process, we calculate the Lyman-dropout feature for our semi-analytic galaxies using a model for IGM absorption. We adopt an effective optical depth of Ly- α absorption at $z < 5.5$ (Fan et al. 2006b),

$$\tau_{\text{eff}} = (0.85 \pm 0.06) \left(\frac{1+z}{5} \right)^{4.3 \pm 0.3}. \quad (10)$$

Fan et al. (2006b) found that the evolution of τ_{eff} significantly accelerates at $z_{\text{abs}} > 5.5$, with the effective optical depth

$$\tau_{\text{eff}} \propto (1+z)^{10.9} \quad (11)$$

at $z=5.5$ – 6.3 . For simplicity, we adopt this relation for all redshifts at $z \geq 5.5$. Although this extrapolation is unphysical, the observed Ly- α flux vanishes at $z > 6$, so that this assumption does not bias the LBG selection.

2.3 Dust attenuation

To compare our luminosities with observations, we need to add the effect of dust attenuation. The rest-frame UV con-

tinuum for a galaxy is assumed to have the form

$$f_\lambda \propto \lambda^\beta, \quad (12)$$

where f_λ is the flux density per wavelength interval and β is the power-law index. For high-redshift galaxies, β can be estimated through photometric SED fitting (Bouwens et al. 2012, 2014b). UV flux can be strongly attenuated by dust grains within galaxies. This is parameterized as

$$F_o(\lambda) = F_i 10^{-0.4A_\lambda}, \quad (13)$$

where F_i and F_o are the intrinsic and observed continuum flux densities respectively, and A_λ is the change in magnitude at rest-frame wavelength λ . The amount of dust attenuation is wavelength dependent with larger optical depths for shorter wavelengths. Dust attenuation therefore reddens the spectrum by steepening the observed spectral slope.

Dust attenuation can be estimated through a variety of indicators such as emission line ratios (e.g. Balmer series), the slope of the rest-frame continuum, the ratio between infrared and UV radiation (Meurer et al. 1999), the stellar mass of galaxies (Pannella et al. 2009; Heinis et al. 2014), and the SFR of galaxies (Reddy et al. 2006). In this work, we adopt a luminosity-dependent dust attenuation model (Bouwens et al. 2012; Smit et al. 2012; Bouwens et al. 2014b) which is summarized below.

Assuming a constant star-formation history, stellar population synthesis shows that galaxies have similar intrinsic UV continuum slopes (e.g. Leitherer & Heckman 1995). The dust-attenuated UV continuum slope, β , of galaxies will therefore reflect the amount of dust attenuation. Meurer et al. (1999) established a relation between UV dust attenuation and observed UV continuum β :

$$A_{1600} = 4.43 + 1.99\beta, \quad (14)$$

where A_{1600} is the dust attenuation at 1600 \AA . This relation is calibrated by comparison with starburst galaxies in the local Universe, assuming that high-redshift galaxies have the same spectral properties as local galaxies (Meurer et al. 1999).

The key observable for determining the dust-attenuation at high redshifts is the value of β for high-redshift galaxies. Observational studies of high-redshift galaxies show that β is larger for galaxies with higher redshifts and lower luminosities (Bouwens et al. 2012, 2014b). Bouwens et al. (2014b) studied this relation using a large sample (>4000 sources) of galaxies at $z \sim 4$ – 8 . They found a piece-wise linear relation between the mean of β and M_{UV} for galaxies at $z \sim 4$ – 6 :

$$\beta = \begin{cases} \frac{d\beta}{dM_{\text{UV}}}(M_{\text{UV,AB}} + 18.8) + \beta_{M_{\text{UV}}=-18.8}, & M_{\text{UV,AB}} \leq -18.8, \\ -0.08(M_{\text{UV,AB}} + 18.8) + \beta_{M_{\text{UV}}=-18.8}, & M_{\text{UV,AB}} > -18.8, \end{cases} \quad (15)$$

where $d\beta/dM_{\text{UV}}$ and $\beta_{M_{\text{UV}}=-18.8}$ are from Table 4 of Bouwens et al. (2014b). We use this piece-wise relation for our model galaxies at $z \sim 5$ and 6.

For galaxies at $z \sim 7$ and 8, we use the linear relation

$$\beta = \frac{d\beta}{dM_{\text{UV}}}(M_{\text{UV,AB}} + 19.5) + \beta_{M_{\text{UV}}=-19.5}, \quad (16)$$

where $d\beta/dM_{\text{UV}}$ and $\beta_{M_{\text{UV}}=-19.5}$ are from Table 3 of Bouwens et al. (2014b).

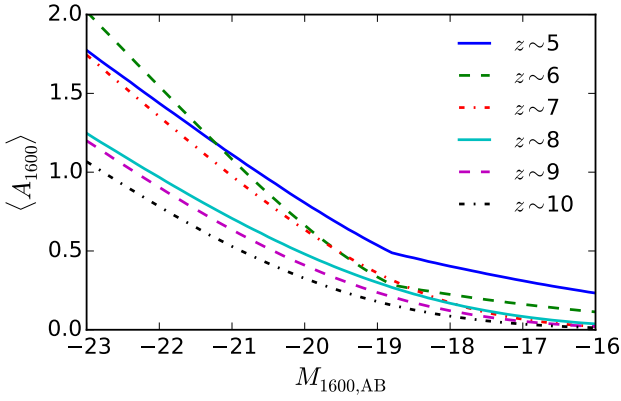


Figure 1. The average dust attenuation at 1600\AA as a function of (dust-attenuated) luminosity at $z \sim 5-10$. The linear relation between A_{1600} and the slope of UV continuum β from Meurer et al. (1999) is used. Rest frame observations for β are from Bouwens et al. (2014b).

Measurements of β at $z \gtrsim 9$ are limited (e.g. Wilkins et al. 2016). We assume that the linear mean β -luminosity dependence in Equation 16 remains valid at $z \sim 9$ and 10. We estimate $\beta_{M_{UV}=-19.5} = -2.19$ and -2.16 for $z \sim 9$ and 10 respectively by linearly fitting the observations (Bouwens et al. 2014b) at $z \sim 4-8$. We set $d\beta/dM_{UV} = -0.16$ for $z \sim 9$ and 10, which equals the mean at $z \sim 4-8$. The uncertainty in this relation is large. However, galaxies at $z > 9$ are usually faint and dust will not significantly attenuate the UV continuum.

We assume β is normally distributed around the mean value with a standard deviation of $\sigma=0.35$ (Bouwens et al. 2014b) at all redshifts. From the linear relation in Equation 14, this means that A_{1600} is also normally distributed. Following Smit et al. (2012), we set $A_{1600}=0$ if $A_{1600}<0$ and then calculate the mean, $\langle A_{1600} \rangle$. Figure 1 shows $\langle A_{1600} \rangle$ as a function of observed (dust-attenuated) luminosity for different redshifts. We can then obtain the relation between $\langle A_{1600} \rangle$ and the intrinsic UV luminosity at 1600\AA using Equation 13. The intrinsic rest-frame magnitude M_{1500}^i and M_{1600}^i are calculated from SEDs using tophat bands which have a width of 100\AA and centres of 1500 and 1600\AA respectively.

Dust attenuation in other UV bands can then be estimated using the reddening curve normalized by $\langle A_{1600} \rangle$. A commonly adopted reddening curve was derived by Calzetti et al. (2000)²:

$$k(\lambda) = \begin{cases} 2.659 \left(-2.156 + \frac{1.509}{\lambda} - \frac{0.198}{\lambda^2} + \frac{0.011}{\lambda^3} \right) + R_V, & 0.12\mu\text{m} \leq \lambda < 0.63\mu\text{m}, \\ 2.659 \left(-1.857 + \frac{1.040}{\lambda} \right) + R_V, & 0.63\mu\text{m} \leq \lambda \leq 2.20\mu\text{m}, \end{cases} \quad (17)$$

² This can also be approximated by a simpler reddening curve with extinction optical depth $\tau_\lambda \propto \lambda^{-0.7}$ at $0.10\mu\text{m} < \lambda < 0.16\mu\text{m}$ (Charlot & Fall 2000).

where the rest-frame wavelength, λ , is in units of μm , $R_V=4.05 \pm 0.80$ is the effective obscuration in the V band, and the coefficients are normalized to $E(B-V) = k(B) - k(V) = 1$. The change of magnitude due to dust attenuation is $A_\lambda = E(B-V)k(\lambda)$. To obtain the A_λ for $\lambda < 0.12\mu\text{m}$, we extrapolate the reddening curve $k(\lambda)$ to $\lambda < 0.12\mu\text{m}$.

2.4 Lyman-Break selection

High-redshift galaxies can be selected using multi-band photometric surveys and the Lyman-break technique. To facilitate direct comparison with observed UV LFs and to study the completeness of LBG selections, we adopt the LBG colour selection criteria from Bouwens et al. (2015b) to select the model galaxies at $z \sim 5-8$:

- The colour selection criterion for $z \sim 5$ is:

$$(V_{606} - i_{775}) > 1.2 \text{ AND } (z_{855} - H_{160} < 1.3) \\ \text{AND } (V_{606} - i_{775} > 0.8(z_{855} - H_{160}) + 1.2). \quad (18)$$

- For $z \sim 6$:

$$(i_{775} - z_{850}) > 1.0 \text{ AND } (Y_{105} - H_{160} < 1.3) \\ \text{AND } (i_{775} - z_{850} > 0.78(Y_{105} - H_{160}) + 1.0). \quad (19)$$

- For $z \sim 7$:

$$(z_{850} - Y_{105}) > 0.7 \text{ AND } (J_{125} - H_{160} < 0.45) \\ \text{AND } (z_{850} - Y_{105} > 0.8(J_{125} - H_{160}) + 0.7). \quad (20)$$

- For $z \sim 8$:

$$(Y_{105} - J_{125}) > 0.45 \text{ AND } (J_{125} - H_{160} < 0.5) \\ \text{AND } (Y_{105} - J_{125} > 0.75(Y_{125} - H_{160}) + 0.525). \quad (21)$$

Here V_{606} , i_{775} , z_{850} , Y_{105} , J_{125} and H_{160} represent the magnitudes in ACS and WFC3/IR filter bands F606W, F775W, F850W, F105W, F125W and F160W respectively. We adopt the colour criteria from Bouwens et al. (2015c) to select the galaxies at $z \sim 9$ and 10:

$$(J_{125} - H_{160} > 0.5) \text{ AND } (H_{160} - [3.6] < 1.4). \quad (22)$$

Here [3.6] represents the magnitude in the *Spitzer*/S-CANDELS $3.6\mu\text{m}$ filter.

We calculate the observed dust-attenuated luminosities in these bands for all model galaxies at $z \sim 5-10$, and pass these through the colour selection criteria. Our model gives the luminosities in dropout bands no matter how faint the galaxies are. We do not want to exclude these faint galaxies, so we do not apply the non-detection criteria. We also do not consider model galaxies at redshifts other than the center of the selection window, and so there is no contamination by interlopers from other redshifts.

Figure 2 shows the LBG colour-colour selection panels. The galaxies in these panels represent a random sample of 5 per cent of the galaxies with $M_{1600} < -15.75$, which are used for our UV LF determination in Figure 3. The galaxies located in the grey regions are selected as star-forming LBG galaxies. The size of the circles represents the UV luminosity of galaxies at rest-frame 1600\AA before dust attenuation is applied.

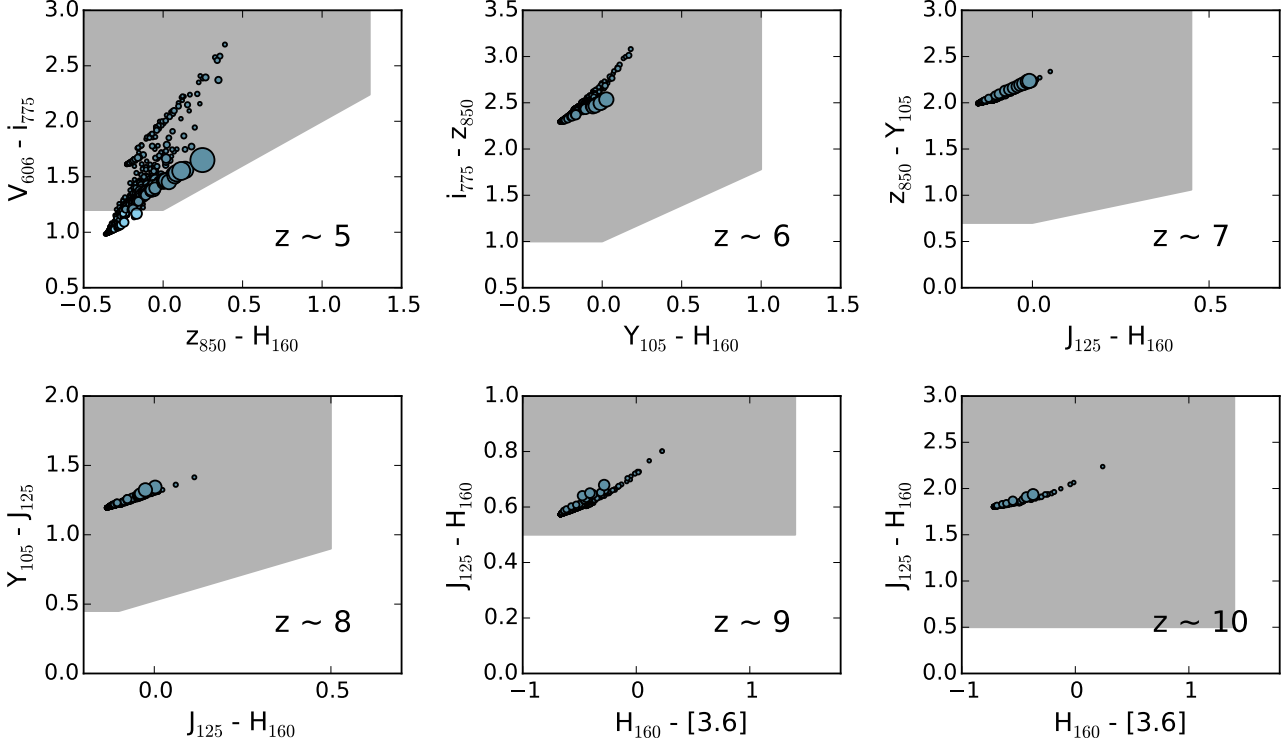


Figure 2. LBG selection criteria used to select star-forming galaxies at $z \sim 5$ – 10 . The blue circles show randomly selected galaxies representing 5 per cent of the total sample with $M_{1600} < -15.75$. The areas of circles are proportional to their observed UV luminosities at rest-frame 1600\AA . The grey-shaded regions are the selection regions for LBGs.

We see that all of our model galaxies are located in the selection regions for $z \sim 6$ – 10 . For $z \sim 5$, a few faint galaxies fall outside of the selection region. The UV-bright galaxies have moved toward the upper-right due to dust attenuation in all panels. Our study shows that if we remove the effect of dust attenuation, a significant number of the brightest galaxies will be located outside of the selection region at $z \sim 5$, where LBG selection for the UV-brightest galaxies is very sensitive to the dust attenuation model.

3 UV LUMINOSITY FUNCTIONS

Figure 3 shows our model UV LFs, $\phi(M_{UV})$, for LBGs (i.e. the galaxies which passed the LBG selection criteria) selected at redshifts $z \sim 5$ – 10 . The observed UV LFs are from Bouwens et al. (2015b) at $z \sim 5, 6, 7, 8$ and 10 , with additional points from Bouwens et al. (2015c) at $z \sim 9$ and 10 .

For the galaxies at $z \sim 5$, we also plot the UV LF for all model galaxies for comparison. We see a slight discrepancy between the LF for all model galaxies and for LBGs, due to the small fraction of faint galaxies with $M_{1600} > -19$ that do not pass the LBG selection criteria. For the galaxies at $z \sim 6$ – 10 , all model galaxies with $M_{1600} < -15.75$ have passed the LBG selection and are identified as LBGs. Our model, which was calibrated to the stellar mass function at $z \sim 5$ – 7 (see Paper-III) produces UV LFs at $z \sim 5$ – 10 that are in excellent agreement with the observations.

We can use the model galaxies to study the shape and

the evolution of UV LFs to much lower luminosities than observed, as shown in Figure 4. To exclude the influence of LBG selection criteria, all model galaxies are used hereafter. The observed LFs from (Bouwens et al. 2015b) and Atek et al. (2015) at $z \sim 7$ are also shown. Atek et al. (2015) obtained the UV LF down to $M_{UV} = -15.25$ at $z \sim 7$. Our prediction is in good agreement with this observation.

We see that the slope of the UV LF remains steep at $M_{1600} < -14$ and becomes flat at $M_{1600} > -14$. The UV LFs have a turnover at $M_{1600} \approx -12$ and then drop towards fainter luminosities. The fact that the faint-end slope remains steep below current detection limits down to $M_{1600} = -14$ has important implications for the photon budget during reionization (see Section 4). The predicted turnover in the number density of faint galaxies can be traced to the condition that the halo mass $\sim 10^8 M_{\odot}$ must exceed the hydrogen cooling limit corresponding to a virial temperature of 10^4 K before stars can form. A larger value of the cooling mass or temperature will lead to a turnover at brighter UV magnitude (e.g. Muñoz & Loeb 2011). This is also seen by comparing to the relation between the mass of dark matter haloes and UV luminosity (as discussed in Section 5.4). The flattening at $M_{1600} > -14$ of LFs is also a testable prediction of the luminosity below which it becomes likely for the halo masses to drop below the hydrogen cooling limit.

We also see that the slope of the UV LFs at $M_{1600} < -16$ steepens towards higher redshift. On the other hand, the slope at fainter magnitudes $-16 < M_{1600} < -10$ does not sig-

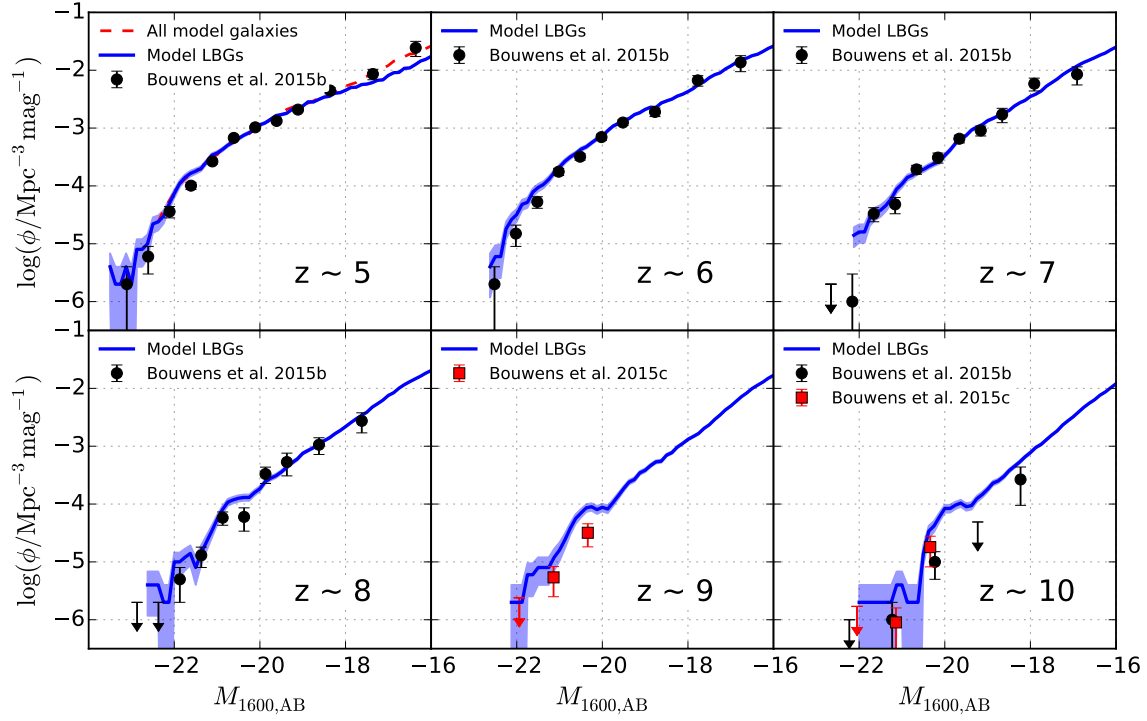


Figure 3. Model UV LFs at $z \sim 5$ – 10 from MERAXES. Blue solid lines show selected LBGs with 1σ Poisson uncertainties shown as shaded regions. Black circles and red squares are observational data from Bouwens et al. (2015b) ($z \sim 5, 6, 7, 8$ and 10) and Bouwens et al. (2015c) ($z \sim 9$ and 10) respectively. The red dashed line at $z \sim 5$ shows the UV LF for all model galaxies without the LBG selection. We see close agreement between the model and observations.

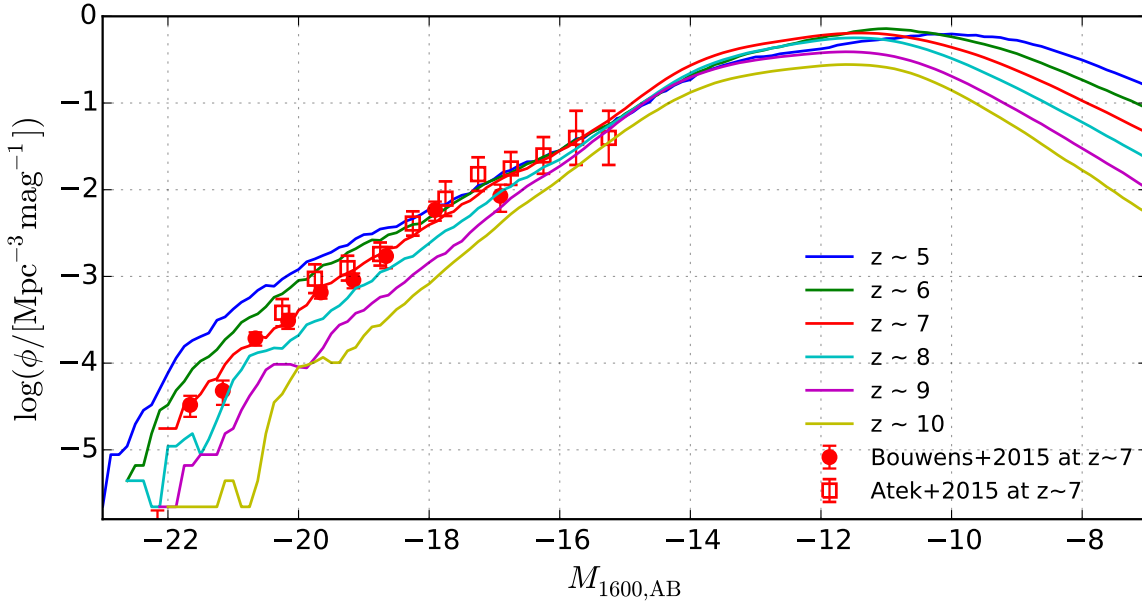


Figure 4. Model UV LFs from MERAXES for all model galaxies extended to low luminosities, illustrating the predicted flattening fainter than $M_{1600} \sim -14$. Red circles and red squares show the observed UV LF from (Bouwens et al. 2015b) and Atek et al. (2015) at $z \sim 7$ respectively.

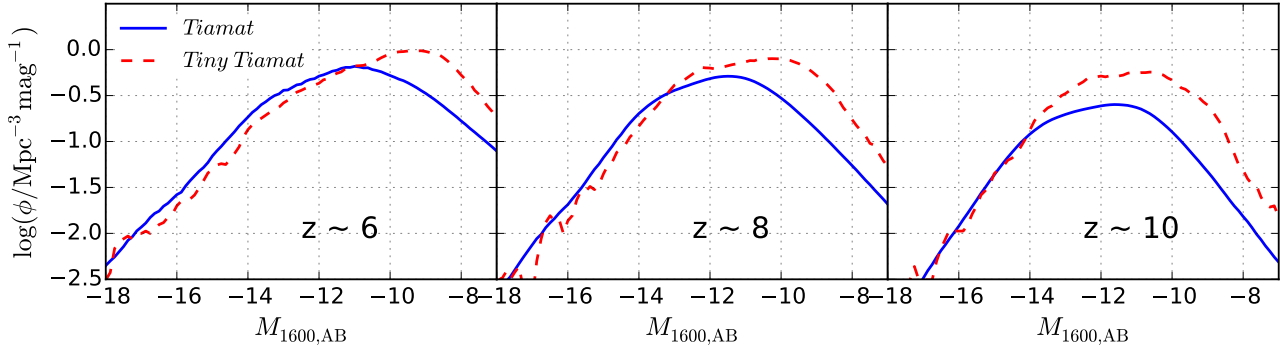


Figure 5. Comparison for UV LFs of all model galaxies based on *Tiamat* and *Tiny Tiamat* simulations at $z \sim 6, 8$ and 10 . The simulation box sizes are $67.8h^{-1}\text{Mpc}$ and $10h^{-1}\text{Mpc}$, and the particle masses are $2.64 \times 10^6 h^{-1}M_{\odot}$ and $6.79 \times 10^4 h^{-1}M_{\odot}$ for *Tiamat* and *Tiny Tiamat* respectively. We see a flattening slope at $M_{\text{UV}} \gtrsim -14$ from both simulations.

nificantly evolve at $z > 5$. We infer that the implied continuous growth of extremely faint LFs reflects the ongoing formation of small haloes.

To investigate how the simulation volume and mass resolution affect the position of the turnover in the UV LF, we compare the predictions based on the *Tiamat* N-body simulation and the much higher mass resolution *Tiny Tiamat* N-body simulation (see Paper-I) in Figure 5. *Tiny Tiamat* has a $10h^{-1}\text{Mpc}$ cubed simulation box and a particle mass of $6.79 \times 10^4 h^{-1}M_{\odot}$, and easily resolves the hydrogen cooling mass at all simulated redshifts. We see that the LFs based on *Tiamat* and *Tiny Tiamat* generally agree at $M_{1600} < -14$. However, the model UV LFs based on *Tiny Tiamat* flatten at $M_{1600} \gtrsim -12$ which is ~ 2 magnitudes fainter than those based on *Tiamat*. This difference quantifies the combined effects of the hydrogen cooling limit not being completely resolved in the *Tiamat* simulation until $z \lesssim 6$, together with merger-triggered star formation in the small haloes near the cooling limit that cannot be resolved by *Tiamat*.

The flattening slope of high-redshift LFs at $M_{\text{UV}} > -14$ has been previously seen in other simulations. For example, O’Shea et al. (2015) carried out a suite of hydrodynamic simulations with an adaptive mesh refinement code (the *Renaissance Simulations*) which employed a self-consistent radiative transfer reionization scheme and included Population III stars (see also Wise et al. 2014, 2012). These simulations have a dark matter particle of $2.9 \times 10^4 M_{\odot}$, and show that the $z > 12$ LF flattens at $M_{\text{UV}} \gtrsim -14$, in good agreement with our results.

4 UV FLUX FROM GALAXIES BELOW THE DETECTION LIMIT

An important quantity for studies of reionization is the ionizing luminosity emitted by the overall population of galaxies. There has been extensive discussion in the literature regarding whether enough star formation has been observed to complete reionization (e.g. Fan et al. 2006a; Robertson et al. 2010, 2013, 2015; Bouwens et al. 2015a). MERAXES describes the stellar mass function of galaxies at $z \sim 5-7$, and the UV LF in the observed range from $z \sim 5-10$. The predicted UV LFs can be used to calculate the UV luminosity density orig-

inating from galaxies above a luminosity threshold L_{lim} :

$$\rho_{\text{UV}} = \int_{L_{\text{lim}}}^{\infty} L\phi(L)dL. \quad (23)$$

The emissivity of galaxies (number of ionizing photons emitted into the IGM per second per comoving volume) can then be estimated using

$$\epsilon = f_{\text{esc}}\xi_{\text{ion}}\rho_{\text{UV}}, \quad (24)$$

where ξ_{ion} is the number of ionizing photons per unit UV luminosity and f_{esc} is the fraction of ionizing photons that escape from the galaxy to ionize the IGM.

Figure 6 shows the emissivity from galaxies brighter than the limit M_{lim} as a fraction of the total emissivity from all galaxies in the simulation at each redshift:

$$\frac{\epsilon_{(\leq M_{\text{lim}})}}{\epsilon_{\text{total}}} = \frac{\int_{-\infty}^{M_{\text{lim}}} \phi(M)L(M)dM}{\int_{-\infty}^{\infty} \phi(M)L(M)dM}. \quad (25)$$

Here we assume f_{esc} is constant for all galaxies at each redshift, although it likely scales with halo mass, possibly compensating for the relative inefficiency in star formation of the faint galaxies (e.g. Wise & Cen 2009; Kuhlen & Faucher-Giguère 2012; Paardekooper et al. 2015). We calculate $\epsilon/\epsilon_{\text{total}}$ for both simulations based on *Tiamat* and *Tiny Tiamat*. *Tiny Tiamat* misses the brightest galaxies due to the limited volume, and so presents conservatively low limits on the total fraction of observed flux. However, we find good agreement between estimates of faint galaxy flux levels among the simulations indicating that our model based on *Tiamat* is not missing significant luminosity.

The luminosity contributions from galaxies brighter than $M_{1600} = -17, -13$ and -10 are shown in Table 1. Under the assumption of an escape fraction of ionizing radiation that does not depend on mass or redshift, this fraction of total luminosity equals the fraction of ionizing photons.

In Figure 6, the *Tiny Tiamat*-based simulation shows a truncation of flux at $M_{\text{UV}} < -20$, indicating that simulation volume influences the flux contribution from the brightest galaxies, especially at $z < 7$. However, both simulations give similar values for fractional flux at $-18 < M_{\text{UV}} < -13$. We find that the fraction of ionizing flux from galaxies brighter than the limit $M_{\text{UV}} = -17$ evolves continuously from 17 per cent at $z \sim 10$ to 58 per cent at $z \sim 5$. This implies that bright

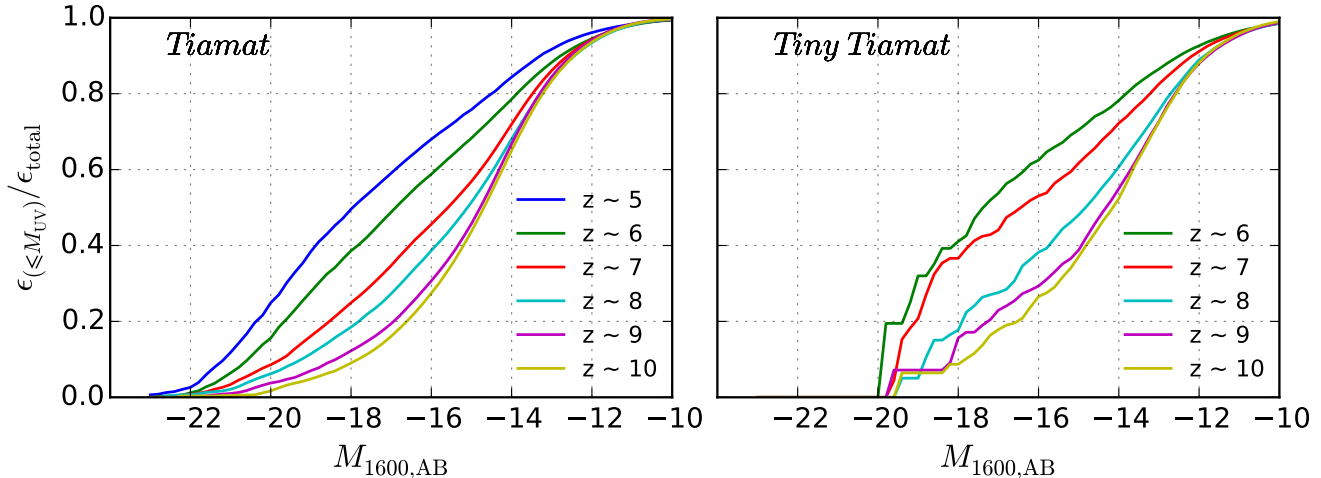


Figure 6. The cumulative fraction of 1600Å UV flux from the model galaxies brighter the luminosity limit M_{1600} based on *Tiamat* (left panel) and *Tiny Tiamat* (right panel) N -body simulations. We see that more than 50 per cent of total UV flux are from galaxies fainter than $M_{UV}=-17$ at $z>6$.

Table 1. The fraction of UV flux at 1600Å above the luminosity limits.

	z	$M_{1600} \leq -17$	$M_{1600} \leq -13$	$M_{1600} \leq -10$
<i>Tiamat</i>	5	0.580	0.916	0.994
	6	0.478	0.884	0.995
	7	0.348	0.866	0.996
	8	0.280	0.845	0.996
	9	0.202	0.850	0.997
	10	0.167	0.840	0.997
<i>Tiny Tiamat</i>	5	-	-	-
	6	0.537	0.861	0.985
	7	0.437	0.821	0.986
	8	0.277	0.756	0.986
	9	0.230	0.729	0.988
	10	0.177	0.725	0.990

galaxies contribute a greater fraction of UV flux at lower redshift than at high redshift. We see that faint galaxies below a detection limit of $M_{UV}=-17$ at $z\sim 6$ (10) provide more than 52 (83) per cent of the total flux, and are therefore likely to be the main source of ionizing photons for reionization. At $z>7$, galaxies with luminosities in the range $-17 < M_{UV} < -13$ provide more than ~ 50 per cent of total UV flux. These results are in agreement with the findings of our hydrodynamic simulations (*Smaug*; see Duffy et al. 2014). Due to their inefficient formation, the faintest galaxies ($M_{UV} > -10$) contribute < 1 per cent ionizing flux at $z\sim 5-10$. Therefore, within the standard model of galaxy formation with a minimum halo mass for star formation as implemented in MERAXES, the UV flux from these faintest galaxies is negligible during the EoR, and a magnitude of $M_{UV}\sim -10$ can be considered as an appropriate integration cutoff for luminosity density calculations.

Before leaving this section, we note that although our model successfully reproduces the galaxy UV luminosity functions, it includes a number of assumptions (e.g., IMF,

dust, metallicity and binary populations) which could affect the UV luminosity of our model galaxies.

5 UV LUMINOSITY-DEPENDENCE OF GALAXY PROPERTIES

In this section, we investigate the relationship between UV luminosity and a series of galaxy properties from our semi-analytic model. This provides us with predictions for these properties towards very low luminosities.

5.1 UV luminosity–SFR relation

Since UV flux comes mostly from massive and short-lived stars, the intrinsic UV luminosity is proportional to SFR and independent of star-formation history over timescales of $t \geq t_{MS}$, where t_{MS} is the main-sequence time of massive stars (Madau et al. 1998). UV luminosity is therefore thought to be a good indicator of SFR (Kennicutt 1998), via the linear relation

$$\frac{\text{SFR}}{M_{\odot}\text{yr}^{-1}} = \mathcal{K}_{UV} \frac{L_{UV}}{\text{erg} \cdot \text{s}^{-1} \cdot \text{Hz}^{-1}}, \quad (26)$$

where the L_{UV} is the intrinsic UV luminosity and \mathcal{K}_{UV} is a constant. The value of \mathcal{K}_{UV} is model dependent, but can be calibrated via a stellar synthesis model which depends on the IMF, metallicity and star-formation history. Using a Salpeter IMF in the range $0.1-125M_{\odot}$ and an exponential burst of star formation with timescale $\gtrsim 1\text{Gyr}$, Madau et al. (1998) obtained $\mathcal{K}_{UV}=1.25 \times 10^{-28}$ for L_{UV} in the wavelength range 1500–2800Å. Assuming 100Myr of constant star formation and a Salpeter IMF in the range $0.1-100M_{\odot}$, Kennicutt (1998) calibrated the value to be $\mathcal{K}_{UV}=1.4 \times 10^{-28}$. Wilkins et al. (2011) similarly obtained a value $\mathcal{K}_{UV}=1.31 \times 10^{-28}$ using the STARBURST99 population synthesis model employed in this paper.

However, at $z \gtrsim 6$ the age of the Universe is less than 1 Gyr, and many galaxies have star-formation histories shorter

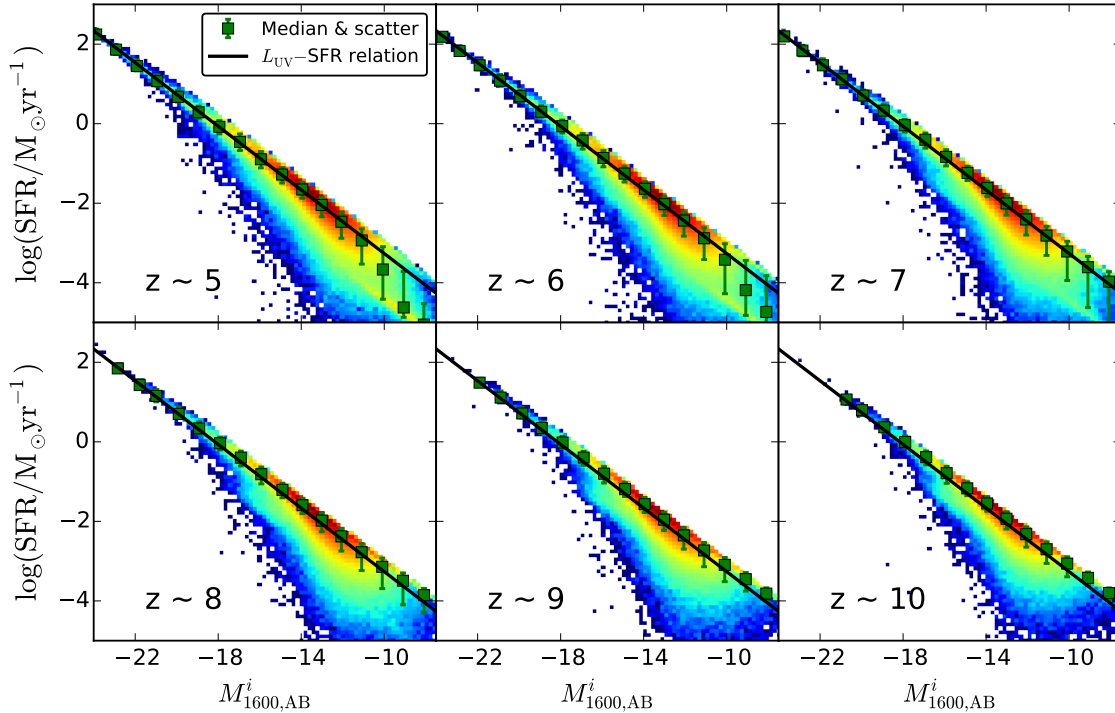


Figure 7. The instantaneous SFR of galaxies as a function of their (unattenuated) intrinsic UV luminosity M_{1600}^i at $z \sim 5-10$. The colour profile represents the logarithm density of the distribution. The green squares and error bars represent the median and 16th to 84th percentiles in bins which contain at least 5 model galaxies respectively. The black lines represent the linear relation between L_{UV} and SFR shown in Equation 26 with $\mathcal{K}_{UV} = 1.25 \times 10^{-28}$ (Kennicutt 1998; Madau et al. 1998). We see that the Madau-Kennicutt conversion describes the correlation between the UV luminosity and the instantaneous SFR from our model well.

than 100 Myr. Therefore, we investigate how well UV luminosity traces the instantaneous SFR using the variable star-formation histories from our model.

Figure 7 shows the relation between the intrinsic UV luminosity and the instantaneous SFR for all galaxies in MERAXES at $z \sim 5-10$. The distribution of SFRs at fixed stellar mass for the galaxies in these plots indicates the effect of variations in star-formation histories. The distribution shows a sharp upper limit, corresponding to the youngest galaxies which formed in the latest snapshot. We see that the model predicts a linear relationship between the UV luminosity and instantaneous SFR, which can be fitted well by the Madau et al. (1998) and Kennicutt (1998) relation. The model galaxy SFRs are distributed with a scatter around the median of $\log(\text{SFR})$ varying from $\sigma \sim 0.2$ dex at $M_{1600}^i < -18$ to ~ 0.3 dex at $M_{1600}^i = -14$. The scatter is larger for UV-faint galaxies than for UV-bright galaxies. The distribution around the median L -SFR relation is not log-normal at faint luminosities in our model owing to the minimum star-formation timescale set by the finite temporal spacing of our simulation snapshots which cuts off the distribution at high SFR. We fit the L -SFR relation using Equation 26 for model galaxies brighter than $M_{UV} = -14$ and obtain $\mathcal{K}_{UV} = (1.13, 1.16, 1.17, 1.19, 1.24, 1.39) \times 10^{-28}$ at $z \sim (5, 6, 7, 8, 9, 10)$. The value of \mathcal{K}_{UV} slightly increases towards higher redshift due to the shorter galaxy-formation

history and the higher fraction of young stars at higher redshift.

5.2 The SFR functions

An important quantity related to the buildup of stellar mass during reionization is the SFR function (e.g. Smit et al. 2012) which is shown in Figure 8. The observed SFR function is estimated by converting the UV LF from Bouwens et al. (2015b,c) using a Kennicutt (1998) and Madau et al. (1998) relation. It is therefore important to investigate whether this assumed conversion introduces bias, and whether the scatter in the relationship effects the determination of the SFR function. We use two methods to derive the model SFR function: (i) we calculate the predicted instantaneous SFR function using the SFR calculated directly from the semi-analytic model; and (ii) to mimic observations, we convert the model UV luminosities to SFRs using Equation 26 with $\mathcal{K}_{UV} = 1.25 \times 10^{-28}$. The LBG selection is implemented for both of the above methods. Figure 8 shows the derived model SFR functions together with the observational estimates.

There is close agreement between the predicted model SFR functions and UV-derived model SFR functions at $\log(\text{SFR}/M_{\odot}\text{yr}^{-1}) > -2$, which in turn agree well with the observational estimates. The small difference between the predicted SFR function for LBGs and the UV derived

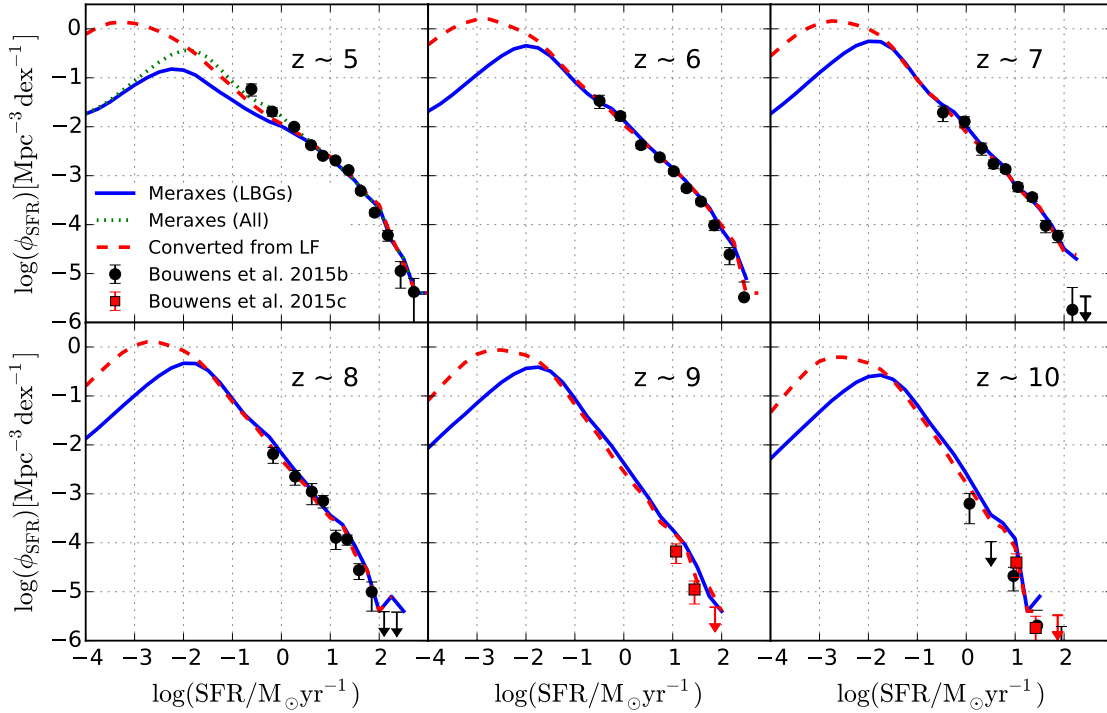


Figure 8. SFR functions of galaxies at $z \sim 5$ – 10 . The blue lines show the SFR function for LBGs obtained directly from the semi-analytic model. The dotted green line is the SFR function obtained from the semi-analytic model but without LBG selection at $z \sim 5$. The red dashed lines show the model SFR converted from UV luminosity using the luminosity–SFR relation with $\mathcal{K}_{\text{UV}} = 1.25 \times 10^{-28}$ (Kennicutt 1998; Madau et al. 1998). Using this relation, black circles show the SFR functions converted from the observed UV LFs from Bouwens et al. (2015b) with dust correction ($z \sim 5, 6, 7, 8$ and 10). Red squares show the SFR functions converted from the observed UV LFs from Bouwens et al. (2015c) ($z \sim 9$ and 10) with dust correction applied. We see close agreement between the SFR functions calculated directly from the model and converted from the predicted UV luminosities.

SFR function at $z \sim 5$ is caused by the LBG colour selection criteria. However, the differences between model-predicted and UV-derived SFR functions at very low SFRs of $\log(\text{SFR}/M_{\odot}\text{yr}^{-1}) < -2$ show that the estimate of the SFR function using the Madau et al. (1998) and Kennicutt (1998) conversion between UV luminosity and SFR will be biased by the scatter of the luminosity–SFR distribution.

5.3 UV luminosity–stellar mass relation

Galaxies which continuously form stars naturally produce a relation between luminosity and stellar mass. Figure 9 shows stellar mass (M_*) as a function of observed UV luminosity (M_{1500}) for model galaxies predicted by MERAXES. We see that our model predicts UV-bright galaxies to have large stellar masses. The model galaxies have stellar masses that are distributed about the median at fixed luminosity with scatter ~ 0.2 – 0.5 dex depending on UV luminosity. For comparison we show the observed relation at $z \sim 5$ – 7 from Duncan et al. (2014), who measured the stellar mass–luminosity relation by fitting the observed photometric data with galaxy model SEDs. To compare with our model, the observational data with nebular emission excluded from the SED fitting is used. We convert the observed data from a Chabrier IMF to a Salpeter IMF by adding 0.24 to $\log(M_*)$ (Duncan et al. 2014). We linearly fit the $\log(M_*)$ – M_{UV} re-

Table 2. The best-fit slopes and intercepts of the median $\log M_*$ – M_{UV} relation (Equation 27) for galaxies with $M_{\text{UV}} \leq -14$.

z	$d \log M_*/dM_{\text{UV}}$	$\log M_*(M_{\text{UV}} = -19.5)$
5	-0.474 ± 0.013	9.21 ± 0.04
6	-0.471 ± 0.021	9.00 ± 0.05
7	-0.477 ± 0.014	8.83 ± 0.04
8	-0.470 ± 0.010	8.68 ± 0.03
9	-0.459 ± 0.012	8.50 ± 0.04
10	-0.456 ± 0.013	8.41 ± 0.05

lation for our bright galaxies with $M_{1500} \leq -14$ using the relation³

$$\log M_* = \frac{d \log M_*}{dM_{\text{UV}}}(M_{\text{UV}} + 19.5) + \log M_*(M_{\text{UV}} = -19.5). \quad (27)$$

The best-fit slopes and intercepts are shown in Table 2 and Figure 10.

At bright luminosities ($M_{1500} \lesssim -14$), the model galaxies are in good agreement with the observed mass–luminosity relation. The best-fit slope (with median ~ -0.47) for model galaxies at $z \sim 5$ – 7 does not significantly change

³ The M_* – L_{UV} relation can be derived by substituting $M_{\text{UV}} = -2.5 \times \log_{10}(L_{\text{UV}}[\text{erg s}^{-1}\text{Hz}^{-1}]) + 51.6$.

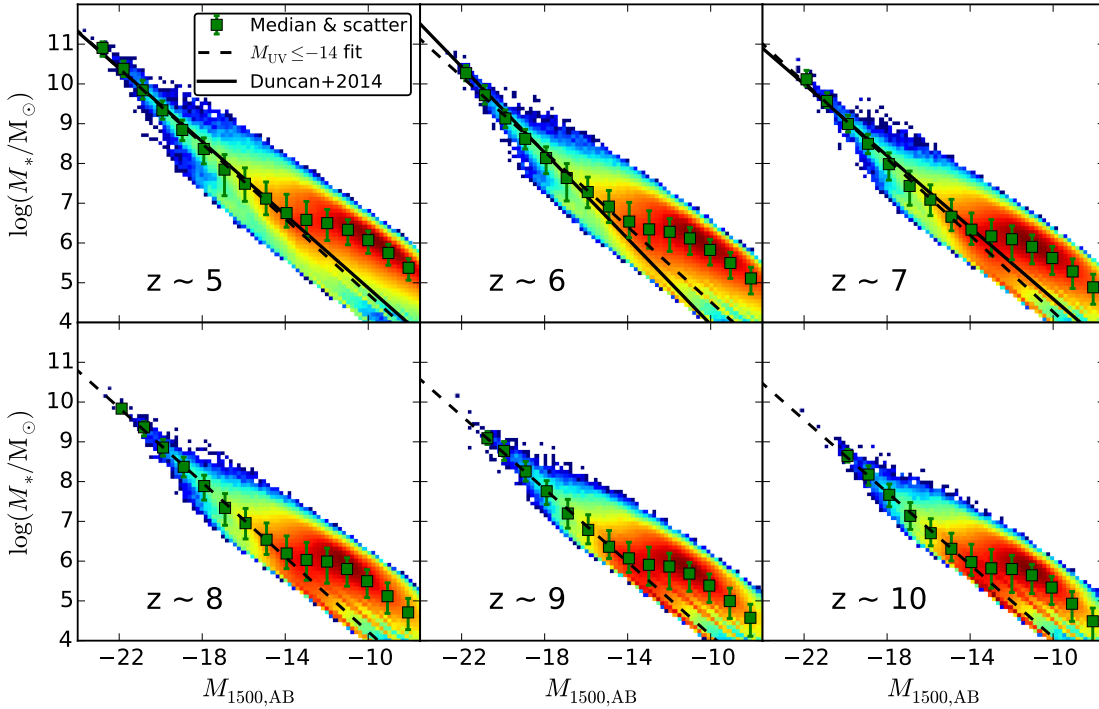


Figure 9. Stellar masses of galaxies as a function of UV luminosity M_{1500} . The colour profile represents the logarithm density of the distribution. The green squares and error bars represent the median and 16th to 84th percentiles in bins which contain at least 5 model galaxies. The black dashed lines are the linear fit to the medians at $M_{1600} \lesssim -14$. The black lines show the observationally fit lines from Duncan et al. (2014), where the stellar mass is converted from a Chabrier IMF to Salpeter IMF by adding 0.24 to $\log(M_*)$. We see a close agreement between our model and observations at $z \sim 5-7$ where the observational data is available.

with redshift, and is close to the observed slopes of $d \log M_*/dM_{UV} \sim -0.45$ to -0.54 from Duncan et al. (2014) at $z \sim 5-7$. Similar slopes are also found by Lee et al. (2012) and Shibuya et al. (2015).

We see that the best-fit intercept $\log M_{*(M_{UV}=-19.5)}$ evolves linearly with redshift. Assuming a constant slope $d \log M_*/dM_{UV} = -0.47$ for the bright galaxies at $z \sim 5-10$, we find the evolution of the luminosity–stellar mass relation can be estimated using the relation

$$\log \left(\frac{M_*}{10^8 M_\odot} \right) = -0.47(M_{1500} + 19.5) - 0.15(z - 7) + 0.86. \quad (28)$$

For fainter galaxies ($-14 < M_{UV} < -11$) the slope of the luminosity–stellar mass relation changes significantly to $d \log M_*/dM_{UV} \sim -0.1$. This flattening of the $\log M_* - M_{UV}$ relation depends on the mass resolution of our dark matter N-body simulations. The relation based on the higher resolution *Tiny Tiamat* simulation flattens at $M_{1500} > -13$ (see Appendix A).

5.4 UV luminosity–halo mass relation

Before concluding, we discuss the relation between the masses of dark matter haloes (identified by the friends of friends procedure, Paper-I) and the UV luminosity of hosted galaxies. If a halo contains more than one galaxy, the luminosity is obtained by summing up all galaxies. Figure 11

Table 3. The best fitting slopes and the intercepts of the median $\log M_{\text{vir}} - M_{UV}$ relation (Equation 29) for galaxies with $M_{UV} \leq -14$.

z	$d \log M_{\text{vir}}/dM_{UV}$	$\log M_{\text{vir},(M_{UV}=-19.5)}$
5	-0.321 ± 0.006	11.05 ± 0.02
6	-0.326 ± 0.006	10.88 ± 0.02
7	-0.345 ± 0.005	10.75 ± 0.02
8	-0.347 ± 0.007	10.63 ± 0.02
9	-0.360 ± 0.008	10.52 ± 0.03
10	-0.366 ± 0.009	10.45 ± 0.03

shows the halo mass–luminosity relation for all model galaxies at $z \sim 5-10$. We see that the UV-bright galaxies tend to be located in massive dark matter haloes. We fit the relation between $\log(M_{\text{vir}})$ and UV magnitude for galaxies brighter than -14 mag at each redshift using a linear relation, as shown by the dashed lines in Figure 11:

$$\log M_{\text{vir}} = \frac{d \log M_{\text{vir}}}{dM_{UV}} (M_{UV} + 19.5) + \log M_{\text{vir},(M_{UV}=-19.5)} \quad (29)$$

The values of the best-fit slopes and intercepts are shown in Table 3 and Figure 12.

We find that the slope of the lines (with median ~ -0.35) slightly steepens towards higher redshift, and the best-fit intercept $\log M_{\text{vir},(M_{UV}=-19.5)}$ evolves linearly with

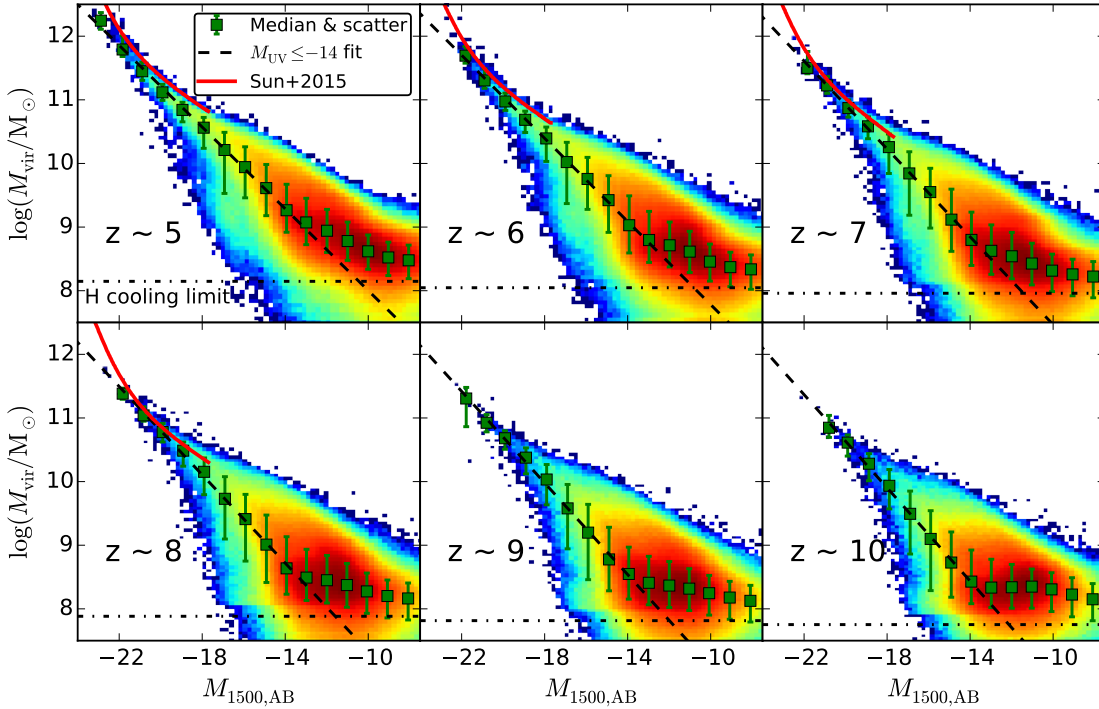


Figure 11. Dark matter halo (FoF group) masses as a function of UV luminosity. The colour profile represents the logarithm density of the distribution. The green squares and errorbars show the median and 16th to 84th percentiles in bins which contain at least 5 galaxies. The black dashed lines are the linear fit to the medians at $M_{1500} \lesssim -14$. The dash-dotted horizontal lines show the hydrogen cooling limit at each redshift. The red solid lines show the relation obtained using halo mass abundance matching technique from Sun & Furlanetto (2015) at $z \sim 5-8$.

redshift. Assuming a constant slope $d \log M_{\text{vir}}/dM_{\text{UV}} = -0.35$ for the UV-bright galaxies at $z \sim 5-10$, we find the evolution of luminosity–halo mass relation can be estimated using

$$\log \left(\frac{M_{\text{vir}}}{10^{10} M_{\odot}} \right) = -0.35(M_{1500} + 19.5) - 0.13(z - 7) + 0.79. \quad (30)$$

The scatter of the distribution at high luminosities is much smaller than at lower luminosities, varying from ~ 0.2 dex at $M_{1500} = -20$ to ~ 0.5 dex at $M_{1500} = -16$. Galaxies with the same UV luminosity tend to be hosted by dark matter haloes with lower masses at higher redshift. This is partly because the stellar populations of galaxies are generally younger at higher redshift. At $z \sim 6$, galaxies with $M_{1500} = -20$ reside in haloes with a mass of $\sim 10^{11.0 \pm 0.1} M_{\odot}$. A detailed analysis of clustering with MERAXES will be presented in Park et al. (2015, in preparation). However, this value is in agreement with the clustering analysis in Barone-Nugent et al. (2014). Figure 11 shows that at the lowest luminosities, halo masses remain constant at $\sim 10^8 M_{\odot}$. This is because the model prevents star formation in haloes below the hydrogen-cooling limit, and explains why the LF turns over at low luminosities. This mass scale is well resolved for the model based on the *Tiny Tiamat* simulation (see Appendix A). We plot the cooling limit for dark matter haloes using the relation between T_{vir} and M_{vir} at high redshifts provided by Barkana & Loeb (2001) and assuming $T_{\text{cool}} = 10^4$ K.

We note that the $\log M_{\text{vir}}-M_{\text{UV}}$ distribution is well described by a linear relation for $-22 < M_{\text{UV}} < -14$ and host halo masses of $M_{\text{vir}} < 10^{12} M_{\odot}$. We do not have a significant sample of $M_{\text{vir}} > 10^{12} M_{\odot}$ haloes, due to the simulation volume and so do not have reliable predictions in that mass range. Moreover, for haloes more massive than $10^{12} M_{\odot}$, AGN feedback, which is not included in the present simulations, may play a significant role in suppressing star formation in galaxies and lead to a steep slope of the $\log M_{\text{vir}}-M_{\text{UV}}$ relation.

The $\log M_{\text{vir}}-M_{\text{UV}}$ relation can also be estimated from observations using the halo abundance matching (HAM) technique (e.g. Vale & Ostriker 2004; Mason et al. 2015; Sun & Furlanetto 2015; Mashian et al. 2016). We plot the $\log M_{\text{vir}}-M_{\text{UV}}$ relation from Sun & Furlanetto (2015) at $z \sim 5-8$ in Figure 11 for comparison with our results. We see that the relations from our model agree with HAM results within statistical uncertainty at $M_{\text{UV}} > -22$. We do see a small difference at $M_{\text{UV}} > -19$ between these two models, which may have arisen from two systematic errors in the HAM methodology: (i) assuming a monotonic relation with an incorrect estimate of scatter between halo mass and galaxy luminosity; (ii) neglecting multiple halo occupation, which leads to the sub-halo luminosities paired with central haloes.

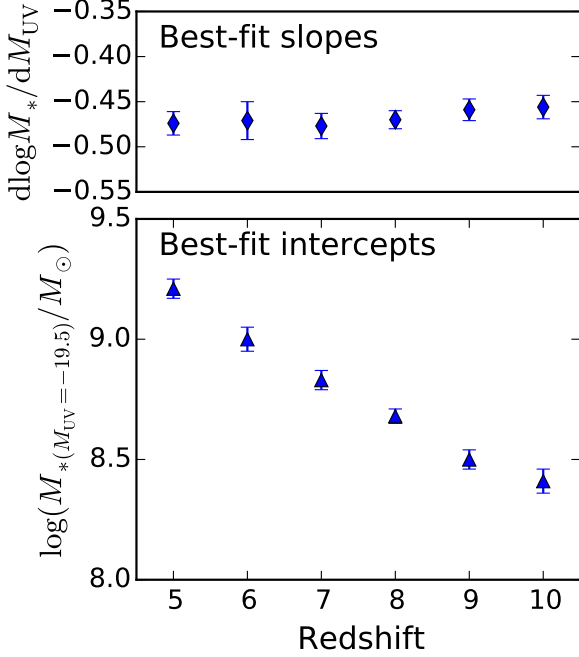


Figure 10. The best fitting slopes (upper panel) and the intercepts at $M_{UV}=-19.5$ (lower panel) of the $\log M_*-M_{UV}$ relation fit to the median trend for galaxies with $M_{UV}\leq-14$.

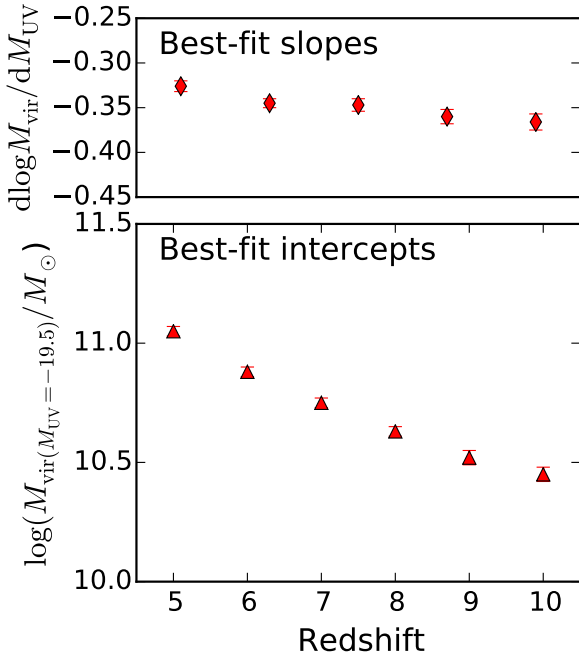


Figure 12. The best fitting slopes (upper panel) and the intercepts at $M_{UV}=-19.5$ (lower panel) of the $\log M_{vir}-M_{UV}$ relation fit to the median trend for galaxies with $M_{UV}\leq-14$.

6 CONCLUSIONS

In this paper we have presented UV LFs for model galaxies during the EoR predicted by the semi-analytic model MERAXES. MERAXES is a new semi-analytic model designed for studying reionization, and includes spatially-dependent UVB feedback as well as time-dependent supernova feedback (Paper-III). By integrating model SEDs with the star formation histories generated from our semi-analytic model, and including Ly α IGM absorption as well as a luminosity-dependent dust attenuation, we derive UV luminosities, M_{1600} , for galaxies at $z\sim 5-10$. We mimic the LBG colour selection processes for our model galaxies, and obtain predictions for observed UV LFs. We also investigate relations between the UV luminosity and a series of galaxy properties including the luminosity-SFR relation, luminosity-stellar mass relation, and the luminosity-halo mass relation. We find that:

(i) Having been calibrated to the stellar mass function at $z\sim 5-7$, our model successfully reproduces the UV LF for high-redshift star-forming galaxies at $z\sim 5-10$. The slope of predicted UV LFs remains steep below current detection limits, and becomes flat at $M_{UV}>-14$ before declining below $M_{UV}\sim-12$. This prediction will be testable in the future based on observations of faint galaxies with *James Webb Space Telescope* and lensing.

(ii) The majority (84–92 per cent) of UV flux at $z\sim 5-10$ is produced in galaxies with $M_{UV}<-13$. At $z\sim 5$, the flux is dominated by the UV-bright galaxies ($M_{UV}\leq-17$). At $z\geq 7$, galaxies with $-17\lesssim M_{UV}\lesssim-13$ are the dominant contributors of UV flux.

(iii) Model galaxies with $M_{UV}\lesssim-14$ are distributed around the luminosity-SFR relation from Kennicutt (1998) and Madau et al. (1998) with a scatter of 0.1–0.3dex. However, we find that the conversion between the high-redshift UV luminosity and SFR functions will be significantly biased by unaccounted-for scatter in the luminosity-SFR distribution for low-SFR galaxies ($SFR<0.01M_\odot\text{yr}^{-1}$).

(iv) Model galaxies with $M_{UV}\leq-14$ have stellar mass to luminosity relations that are consistent with the observed relations from Duncan et al. (2014) at $z\sim 5-7$. The $\log(M_*)-M_{UV}$ relation has a slope of ~-0.47 .

(v) For high-mass dark matter haloes, there is a linear relation between $\log(M_{vir})$ and M_{UV} with a slope of ~-0.35 . The scatter in this relation decreases with increasing luminosity. Galaxies with luminosities of $M_{UV}=-20$ at $z\sim 6$ are hosted in dark matter haloes of mass $M_{vir}\sim 10^{11.0\pm 0.1}M_\odot$. This mass decreases linearly towards higher redshift until $z\sim 9$.

In summary, the MERAXES semi-analytic model successfully describes the observed build up of the stellar mass of galaxies during reionization as recorded in the redshift-dependent luminosity functions and stellar mass functions. This gives us confidence in extrapolating the model to redshifts and luminosities beyond current observations. Future papers will apply MERAXES to a series of additional observables during EoR including the morphology of 21-cm emission from the IGM (Geil et al. 2015, Paper-V) and galaxy sizes and clustering.

ACKNOWLEDGMENTS

This research was supported by the Victorian Life Sciences Computation Initiative (VLSCI), grant ref. UOM0005, on its Peak Computing Facility hosted at the University of Melbourne, an initiative of the Victorian Government, Australia. Part of this work was performed on the gSTAR national facility at Swinburne University of Technology. gSTAR is funded by Swinburne and the Australian Governments Education Investment Fund. This research program is funded by the Australian Research Council through the ARC Laureate Fellowship FL110100072 awarded to JSBW. AM acknowledges support from the European Research Council (ERC) under the European Unions Horizon 2020 research and innovation program (grant agreement No 638809 AIDA).

REFERENCES

- Angel P. W., Poole G. B., Ludlow A. D., Duffy A. R., Geil P. M., Mutch S. J., Mesinger A., Wyithe J. S. B., 2015, arXiv:1512.00560
- Atek H. et al., 2015, *ApJ*, 814, 69
- Barkana R., Loeb A., 2001, *Phys. Rep.*, 349, 125
- Barone-Nugent R. L. et al., 2014, *ApJ*, 793, 17
- Baugh C. M., 2006, *Reports on Progress in Physics*, 69, 3101
- Bouwens R. J. et al., 2014a, *ApJ*, 795, 126
- Bouwens R. J., Illingworth G. D., Franx M., Ford H., 2007, *ApJ*, 670, 928
- Bouwens R. J., Illingworth G. D., Oesch P. A., Caruana J., Holwerda B., Smit R., Wilkins S., 2015a, *ApJ*, 811, 140
- Bouwens R. J. et al., 2012, *ApJ*, 754, 83
- Bouwens R. J. et al., 2011, *ApJ*, 737, 90
- Bouwens R. J. et al., 2014b, *ApJ*, 793, 115
- Bouwens R. J. et al., 2010, *ApJ*, 709, L133
- Bouwens R. J. et al., 2015b, *ApJ*, 803, 34
- Bouwens R. J. et al., 2015c, arXiv:1506.01035
- Bower R. G., Benson A. J., Malbon R., Helly J. C., Frenk C. S., Baugh C. M., Cole S., Lacey C. G., 2006, *MNRAS*, 370, 645
- Bruzual G., Charlot S., 2003, *MNRAS*, 344, 1000
- Calzetti D., Armus L., Bohlin R. C., Kinney A. L., Koornneef J., Storchi-Bergmann T., 2000, *ApJ*, 533, 682
- Charlot S., Fall S. M., 2000, *ApJ*, 539, 718
- Cole S., Aragon-Salamanca A., Frenk C. S., Navarro J. F., Zepf S. E., 1994, *MNRAS*, 271, 781
- Cole S., Lacey C. G., Baugh C. M., Frenk C. S., 2000, *MNRAS*, 319, 168
- Croton D. J. et al., 2006, *MNRAS*, 365, 11
- Duffy A. R., Wyithe J. S. B., Mutch S. J., Poole G. B., 2014, *MNRAS*, 443, 3435
- Duncan K. et al., 2014, *MNRAS*, 444, 2960
- Fall S. M., Efstathiou G., 1980, *MNRAS*, 193, 189
- Fan X., Carilli C. L., Keating B., 2006a, *ARA&A*, 44, 415
- Fan X. et al., 2006b, *AJ*, 132, 117
- Finkelstein S. L. et al., 2012, *ApJ*, 756, 164
- Geil P. M., Mutch S. J., Poole G. B., Angel P. W., Duffy A. R., Mesinger A., Wyithe J. S. B., 2015, arXiv:1512.00564
- González V., Labbé I., Bouwens R. J., Illingworth G., Franx M., Kriek M., 2011, *ApJ*, 735, L34
- Gonzalez-Perez V., Lacey C. G., Baugh C. M., Lagos C. D. P., Helly J., Campbell D. J. R., Mitchell P. D., 2014, *MNRAS*, 439, 264
- Grazian A. et al., 2015, *A&A*, 575, A96
- Heinis S. et al., 2014, *MNRAS*, 437, 1268
- Kauffmann G., Colberg J. M., Diaferio A., White S. D. M., 1999, *MNRAS*, 303, 188
- Kauffmann G., White S. D. M., Guiderdoni B., 1993, *MNRAS*, 264, 201
- Kennicutt, Jr. R. C., 1998, *ARA&A*, 36, 189
- Kuhlen M., Faucher-Giguère C.-A., 2012, *MNRAS*, 423, 862
- Lacey C. G., Baugh C. M., Frenk C. S., Benson A. J., 2011, *MNRAS*, 412, 1828
- Lacey C. G. et al., 2015, arXiv:1509.08473
- Lee K.-S. et al., 2012, *ApJ*, 752, 66
- Leitherer C., Ekström S., Meynet G., Schaerer D., Agienko K. B., Levesque E. M., 2014, *ApJS*, 212, 14
- Leitherer C., Heckman T. M., 1995, *ApJS*, 96, 9
- Leitherer C., Ortiz Otálvaro P. A., Bresolin F., Kudritzki R.-P., Lo Faro B., Pauldrach A. W. A., Pettini M., Rix S. A., 2010, *ApJS*, 189, 309
- Leitherer C. et al., 1999, *ApJS*, 123, 3
- Madau P., Pozzetti L., Dickinson M., 1998, *ApJ*, 498, 106
- Mashian N., Oesch P. A., Loeb A., 2016, *MNRAS*, 455, 2101
- Mason C. A., Trenti M., Treu T., 2015, *ApJ*, 813, 21
- McLure R. J. et al., 2013, *MNRAS*, 432, 2696
- McLure R. J., Dunlop J. S., Cirasuolo M., Koekemoer A. M., Sabbi E., Stark D. P., Targett T. A., Ellis R. S., 2010, *MNRAS*, 403, 960
- Mesinger A., Furlanetto S., 2007, *ApJ*, 669, 663
- Mesinger A., Furlanetto S., Cen R., 2011, *MNRAS*, 411, 955
- Meurer G. R., Heckman T. M., Calzetti D., 1999, *ApJ*, 521, 64
- Mo H. J., Mao S., White S. D. M., 1998, *MNRAS*, 295, 319
- Muñoz J. A., Loeb A., 2011, *ApJ*, 729, 99
- Mutch S. J., Geil P. M., Poole G. B., Angel P. W., Duffy A. R., Mesinger A., Wyithe J. S. B., 2015, arXiv:1512.00562
- Mutch S. J., Poole G. B., Croton D. J., 2013, *MNRAS*, 428, 2001
- Oesch P. A. et al., 2010, *ApJ*, 709, L16
- Oke J. B., Gunn J. E., 1983, *ApJ*, 266, 713
- O’Shea B. W., Wise J. H., Xu H., Norman M. L., 2015, *ApJ*, 807, L12
- Paardekooper J.-P., Khochfar S., Dalla Vecchia C., 2015, *MNRAS*, 451, 2544
- Pannella M. et al., 2009, *ApJ*, 698, L116
- Planck Collaboration et al., 2015, arXiv:1502.01589
- Poole G. B., Angel P. W., Mutch S. J., Power C., Duffy A. R., Geil P. M., Mesinger A., Wyithe S. B., 2015, arXiv:1512.00559
- Reddy N. A., Steidel C. C., Fadda D., Yan L., Pettini M., Shapley A. E., Erb D. K., Adelberger K. L., 2006, *ApJ*, 644, 792
- Robertson B. E., Ellis R. S., Dunlop J. S., McLure R. J., Stark D. P., 2010, *Nature*, 468, 49
- Robertson B. E., Ellis R. S., Furlanetto S. R., Dunlop J. S., 2015, *ApJ*, 802, L19
- Robertson B. E. et al., 2013, *ApJ*, 768, 71

Salpeter E. E., 1955, *ApJ*, 121, 161
 Schaye J. et al., 2015, *MNRAS*, 446, 521
 Schaye J. et al., 2010, *MNRAS*, 402, 1536
 Schenker M. A. et al., 2013, *ApJ*, 768, 196
 Schmidt K. B. et al., 2014, *ApJ*, 786, 57
 Shibuya T., Ouchi M., Harikane Y., 2015, *ApJS*, 219, 15
 Smit R., Bouwens R. J., Franx M., Illingworth G. D., Labbé I., Oesch P. A., van Dokkum P. G., 2012, *ApJ*, 756, 14
 Sobacchi E., Mesinger A., 2013a, *MNRAS*, 432, 3340
 Sobacchi E., Mesinger A., 2013b, *MNRAS*, 432, L51
 Somerville R. S., Hopkins P. F., Cox T. J., Robertson B. E., Hernquist L., 2008, *MNRAS*, 391, 481
 Somerville R. S., Primack J. R., Faber S. M., 2001, *MNRAS*, 320, 504
 Song M. et al., 2015, arXiv:1507.05636
 Springel V. et al., 2005, *Nature*, 435, 629
 Steidel C. C., Adelberger K. L., Giavalisco M., Dickinson M., Pettini M., 1999, *ApJ*, 519, 1
 Steidel C. C., Giavalisco M., Pettini M., Dickinson M., Adelberger K. L., 1996, *ApJ*, 462, L17
 Sun G., Furlanetto S. R., 2015, arXiv:1512.06219
 Sutherland R. S., Dopita M. A., 1993, *ApJS*, 88, 253
 Vale A., Ostriker J. P., 2004, *MNRAS*, 353, 189
 Vázquez G. A., Leitherer C., 2005, *ApJ*, 621, 695
 Weisz D. R., Johnson B. D., Conroy C., 2014, *ApJ*, 794, L3
 White S. D. M., Frenk C. S., 1991, *ApJ*, 379, 52
 White S. D. M., Rees M. J., 1978, *MNRAS*, 183, 341
 Wilkins S. M., Bouwens R. J., Oesch P. A., Labbé I., Sargent M., Caruana J., Wardlow J., Clay S., 2016, *MNRAS*, 455, 659
 Wilkins S. M., Bunker A. J., Lorenzoni S., Caruana J., 2011, *MNRAS*, 411, 23
 Wise J. H., Cen R., 2009, *ApJ*, 693, 984
 Wise J. H., Demchenko V. G., Halicek M. T., Norman M. L., Turk M. J., Abel T., Smith B. D., 2014, *MNRAS*, 442, 2560
 Wise J. H., Turk M. J., Norman M. L., Abel T., 2012, *ApJ*, 745, 50

APPENDIX A: LUMINOSITY—MASS RELATIONS BASED ON *TINY TIAMAT*

In this appendix we present the luminosity–stellar mass relation, and luminosity–halo mass relations based on the high-resolution *Tiny Tiamat* simulation in order to investigate whether the flattening at low luminosities seen in Figure 9 and Figure 11 was due to resolution effects. Figure A1 shows the $\log M_* - M_{UV}$ relation for the model based on *Tiny Tiamat*. We linearly fit the relation for the bright galaxies with $M_{1500} \lesssim -14$. The best-fit slopes and intercepts are shown in Table A1. The best-fit slopes are larger than the slopes from the model based on *Tiamat*. The relation becomes flat at $M_{1500} > -13$ which is 1 magnitude fainter than the model based on *Tiamat*.

Figure A2 shows the halo mass–luminosity relation for all model galaxies based on *Tiny Tiamat* at $z \sim 5-10$. We fit the $\log(M_{vir})$ and the UV magnitudes for galaxies brighter than -14 mag at each redshift using a linear relation, as shown by the dashed lines in Figure A2. The values of best-fit slopes and intercepts are shown in Table A2. The fig-

Table A1. The best fitting slopes and the intercepts of the $\log M_* - M_{UV}$ relation for galaxies with $M_{UV} \leq -14$ based on the *Tiny Tiamat* N-body simulation.

z	$d \log M_* / dM_{UV}$	$\log M_{*(M_{UV}=-19.5)}$
6	-0.447 ± 0.016	8.94 ± 0.05
7	-0.424 ± 0.015	8.71 ± 0.05
8	-0.435 ± 0.029	8.63 ± 0.11
9	-0.405 ± 0.017	8.42 ± 0.06
10	-0.437 ± 0.009	8.49 ± 0.04

Table A2. The best fitting slopes and the intercepts of the $\log M_{vir} - M_{UV}$ relation for galaxies with $M_{UV} \leq -14$ based on the *Tiny Tiamat* N-body simulation.

z	$d \log M_{vir} / dM_{UV}$	$\log M_{vir, (M_{UV}=-19.5)}$
6	-0.290 ± 0.009	10.86 ± 0.03
7	-0.325 ± 0.018	10.84 ± 0.07
8	-0.365 ± 0.019	10.86 ± 0.07
9	-0.319 ± 0.024	10.46 ± 0.09
10	-0.379 ± 0.006	10.61 ± 0.02

ure clearly shows that the model prevents star formation in haloes below the hydrogen-cooling limit.

In summary, the conclusions regarding relations between luminosity and stellar or halo mass are not an artifact of simulation resolution. We do find that there are small differences in the predicted luminosities within the smallest haloes, owing to the additional star formation in the merger triggered starburst phase.

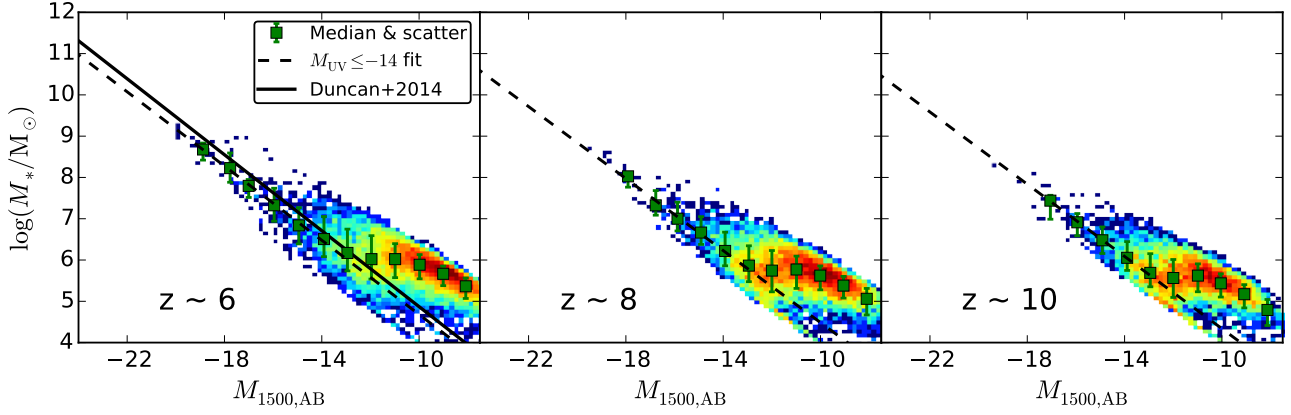


Figure A1. Same as Figure 9 but for model galaxies at $z \sim 6, 8$ and 10 based on the *Tiny Tiamat* N-body simulation, which has a smaller volume but higher mass resolution than the *Tiamat* simulation.

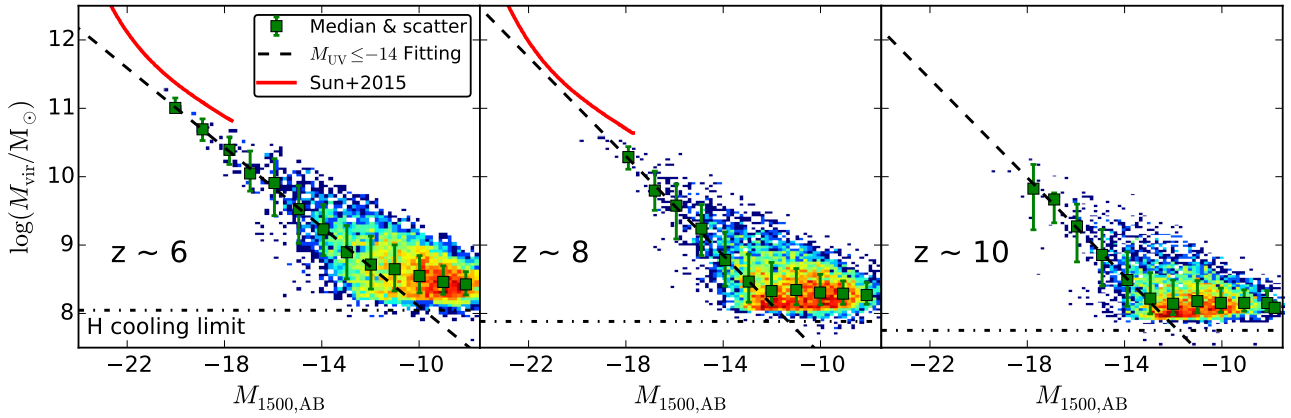


Figure A2. Same as Figure 11 but for model galaxies at $z \sim 6, 8$ and 10 based on the *Tiny Tiamat* N-body simulation, which has a smaller volume but higher mass resolution than the *Tiamat* simulation.

This paper has been typeset from a \LaTeX file prepared by the author.